Taylor & Francis
Taylor & Francis Group

Particulate Science and Technology
An International Journal

ISSN: 0272-6351 (Print) 1548-0046 (Online) Journal homepage: http://www.tandfonline.com/loi/upst20

Simulated airflow and rigid fiber behavior in a realistic nasal airway model

Kevin T. Shanley, Goodarz Ahmadi, Philip K. Hopke & Yung-Sung Cheng

To cite this article: Kevin T. Shanley, Goodarz Ahmadi, Philip K. Hopke & Yung-Sung Cheng (2018) Simulated airflow and rigid fiber behavior in a realistic nasal airway model, Particulate Science and Technology, 36:2, 131-140, DOI: 10.1080/02726351.2016.1208694

To link to this article: https://doi.org/10.1080/02726351.2016.1208694

Accepted author version posted online: 12 Jul 2016.
Published online: 10 Sep 2016.

PARTICULATE SCIENCE AND TECHNOLOGY
2018, VOL. 36, NO. 2, 131–140
http://dx.doi.org/10.1080/02726351.2016.1208694

Taylor & Francis
Taylor & Francis Group

Simulated airflow and rigid fiber behavior in a realistic nasal airway model

Kevin T. Shanley[a], Goodarz Ahmadi[b], Philip K. Hopke[c], and Yung-Sung Cheng[d]

[a]Division of Engineering Programs, SUNY New Paltz, New Paltz, NY, USA; [b]Department of Mechanical and Aeronautical Engineering, Clarkson University, Potsdam, NY, USA; [c]Department of Chemical and Biomolecular Engineering, Clarkson University, Potsdam, NY, USA; [d]Lovelace Respiratory Research Laboratory, Albuquerque, NM, USA

ABSTRACT

Particles may become airborne due to numerous natural and anthropogenic processes. The nose provides protection for the respiratory system through deposition that prevents particles from reaching more sensitive regions. A series of simulations have been conducted to better predict the deposition efficiency within the nasal passages. Computational fluid dynamics coupled with Lagrangian particle tracking have been used to estimate the deposition of both fibrous and spherical particles. MRI data was collected from the left and right passages of an adult male of mass 120.2 kg and height 181.6 cm. The two passages were constructed into separate computational volumes consisting of approximately 950,000 unstructured polyhedral cells each. A steady, incompressible, laminar flow model was used to simulate the inhalation portion of a human breathing cycle. Volumetric flow rates were varied to represent the full range of human nasal breathing. Qualitatively, the simulated airflow field was shown to agree well with previously published in vitro studies on different nasal replicas. An empirical expression for pressure drop as a function of flow rate that takes the form of Rohrer's equation is proposed based on the measured data. Deposition efficiency was shown to depend on fiber aspect ratio, particle size, and flow rate. Nasal geometry was also identified as a key factor affecting deposition. A modified Stokes number is proposed along with a novel empirical expression for fiber deposition efficiency in the nasal airway.

KEYWORDS

CFD; fiber motion; human nose; Lagrangian particle tracking; nasal breathing; particle deposition efficiency

Introduction

Among other functions, the human nose serves to remove particles from inhaled air. This function protects the lungs and more sensitive regions of the respiratory tract from damage due to particle deposition. The original investigation into the human nasal airway deposition was performed by Swift and Proctor (1977) with in vitro experiments on a cast reconstructed from a mold taken from a cadaver. A miniature pitot tube was used in different locations within their life-sized nasal passage replica to obtain velocity measurements. Considerable understanding of the flow field inside the human nose was gained from this study. Guilmette, Wicks, and Wolff (1989) determined, however, that this model generation method provides a less than accurate representation of the cavity of a living human as the airways are prone to collapse shortly after death.

Imaging technology such as Magnetic Resonance Imaging (MRI) and Computed Tomography (CT) has improved data accuracy significantly. These minimally invasive procedures are able to digitally capture two- and three-dimensional slice data of the airway geometry. The first such use for production of a nasal replica was Swift (1991). He took MRI scans of a healthy, nonsmoking, 53-year-old, Caucasian male with mass 73 kg and height 173 cm. At least six studies have reported using this data (i.e., Swift 1991; Swift et al. 1992; Guilmette et al. 1994; Subramanian et al. 1998; Kelly, Prasad, and Wexler 2000, 2004a, 2004b; Lu et al., 2007).

Swift (1991) produced the first replica with this data from a number of 3-mm-thick plastic sandwich elements that were manually carved with a high-speed cutting tool of unspecified diameter or size. Tracings of airway outlines on the plastic elements were used for guidance in the manufacturing process. A miniature pitot tube was again used to take velocity measurements in various locations within the model. A steady inspiratory flow was used.

Swift et al. (1992) measured the deposition of particles in replicate cast models of the human nasal cavity in three different laboratories for a range of particle sizes from 0.6 to 200 nm. These measurements were conducted over a range of flow rates from 1.4 to 28.7 L/min (50 L/min for sizes from 4.6 to 200 nm) using radon and thoron decay product aerosols as well as larger ultrafine particles. At that time, these results represented the best estimate of the diffusional deposition of ultrafine particles in the human nasal cavity.

Guilmette et al. (1994), Kelly, Prasad, and Wexler (2000), and Kelly et al. (2004a, 2004b) used different and more precise manufacturing processes to generate nasal airway flow volumes from the Swift (1991) data. Their efforts produced models that more accurately represented the subject's nasal airways. They also showed that the method of manufacture (i.e., the precision with which the model was manufactured) had a significant influence on the experimental results. They also concluded that this implied anatomy had a significant influence on particle deposition rates.

CONTACT Kevin T. Shanley shanleyk@newpaltz.edu Division of Engineering Programs, SUNY New Paltz, New Paltz, NY, USA.
Color versions of one or more of the figures in the article can be found online at www.tandfonline.com/upst.

Subramanian et al. (1998) used CAD (computer-aided design) software to identify key perimeter coordinates and stitch the coronal cross sections together into a 3D volume. This same method was employed to generate the models discussed in this work.

Most recently, the MRI scans of Swift (1991) were used by Liu et al. (2007) to create a computational model. They loaded the scan data into a 3D volume generation software package and obtained a 3D surface triangulation. A volume mesh was then created from the surface model. The Finite Element Method (FEM) was used to numerically solve a steady airflow field inside the nasal airway. Reynolds Averaged Navier–Stokes (RANS) and Large Eddy Simulations (LES) turbulence models were used to better represent the flow field.

While the details vary slightly among different studies, they all share qualitative agreement. All measurements in the literature reported that the flow is laminar for low-to-moderate breathing rates ($\leq$25 L/min). Swift and Proctor (1977) and Schreck et al. (1993) reported observing vortices posterior to the nasal valve. The LES results of Liu et al. (2007) confirmed a peak in turbulence intensity in precisely the same location. All investigators reported the maximum axial velocity to occur in the nasal valve (e.g., Swift and Proctor 1977; Guilmette, Wicks, and Wolff 1989; Swift 1991; Swift et al. 1992; Guilmette et al. 1994; Subramanian et al. 1998; Kelly, Prasad, and Wexler 2000, 2004a, 2004b; Liu et al. 2007).

Shi, Kleinstreuer, and Zhang (2006) challenged the assumption that inhaled airflow was steady. Their work investigated steady inhalation as well as the acceleration and deceleration phases of an idealized breathing cycle. They found under transient flow conditions nanoparticles deposited less frequently than under steady flow conditions with the same mean inlet velocity. Shi, Kleinstreuer, and Zhang (2007), (2008) studied the micro and nano-particles deposition in nasal cavity and also included the effect of surface roughness.

Dai et al. (2006) showed particles having aerodynamic diameter, $d_{ae} = d_{p(}\rho_p/\rho_{\mathrm{H2O}})^{0.5}$, up to 135 μm could be inhaled by some human subjects when concentrations near the nostril were large enough. However, particles having diameter less than 10 μm (PM_{10}) have been identified as posing the greatest risks to human health (Pope 2000; U.S. Environmental Protection Agency [USEPA], 1996). Once entering the nasal airways, these particles have a greater probability of passing through and entering into the lungs.

Tu, Inthavong, and Ahmadi (2013) published a comprehensive review of in vivo, in vitro, and numerical experiments on particle transport and deposition in the human nasal airway. Applications of computational simulations as an aid to nasal surgical applications were described by Moghadas et al. (2011) and Abouali et al. (2012). Dispersion of particles in nasal passage and upper airways under turbulent flow regime was studied by Ghahramani et al. (2014).

A detailed analysis of published in vivo and in vitro experiments by Cheng (2003) and Cheng et al. (2001a and 2001b) resulted in an empirical expression for deposition of inertial particles. Impaction deposition efficiency is expressed as a function of Stokes number and was able to collapse data from adults and children onto the same curve.

Because fibrous materials have been associated with potentially elevated toxicity, recent effort has been invested to understand their deposition efficiency in the human nasal airway. The anisotropic shape of a fiber makes the physics considerably more complicated. The forces acting on the fiber are a function of the fiber's orientation with respect to the direction of the local flow field. Asgharian and Anjilvel (1995), Fan and Ahmadi (1995), and Shanley and Ahmadi (2011) derive the expressions for describing the motion of a suspended fiber. Asgharian and Anjilvel (1995) described the motions of a fiber by defining its Euler angles. Shanley and Ahmadi (2011) implemented this formulation into the commercial CFD solver FLUENT so it could be applied to generalized flow fields. Fan and Ahmadi (1995) took an alternative approach and described fiber motion by defining its Euler variables. The results of all three were shown to have very good agreement.

The first report on fiber deposition in the nasal airway was an in vitro study on a replica cast published by Su and Cheng (2005). They examined deposition of uniform diameter carbon fibers with polydisperse lengths, under steady inspiratory flow. In general, fibers deposited with less frequency than comparably sized spheres. Impaction was identified as the primary deposition mechanism as deposition efficiency increased with inertia.

Su et al. (2008) studied the deposition of carbon, glass, and titanium dioxide fibers on a nasal airway replica cast. They introduced a concentration of uniform diameter fibers with polydisperse lengths for each material. It was shown that carbon fibers were trapped with greater frequency than the glass or titanium dioxide fibers. Notably, a significant majority of fibers independent of material were collected in the vestibule.

Wang et al. (2008) performed in vitro experiments on stereo lithography (SL) replicas of three human nasal airways. Model I was the same model used in the numerical experiments of Zamankhan et al. (2006) and Shanley et al. (2008). Models II and III were constructed from the same MRI data as the models constructed for the simulations described herein. In these earlier works, a novel approach was used to parameterize the data. The proposed parameter was the product of Stokes number and dimensionless particle relaxation time. Stokes number was dependent on nostril surface area while particle relaxation was dependent on valve hydraulic diameter and distance from the nasopharynx. All data sets collapsed roughly onto a single curve and an empirical expression was proposed.

Numerical studies on fiber transport and deposition are scarcer than their in vitro counterparts. The mathematical expressions governing the motion of a fiber are complex making implementation difficult and computations costly. Using empirical correlations to modify the drag coefficient on a sphere, Inthavong et al. (2008) simulated the deposition of fibers in a nasal airway. They found that the general trends of their simplified model prediction to match with the data of Su and Cheng (2005).

In the current study, a series of numerical experiments were conducted to quantify the airflow and particle deposition in the human nasal airway. MRI data was collected from the left (Model I) and right (Model II) passages of a human male of mass 120.2 kg and height 181.6 cm. The two passages were constructed into separate computational volumes consisting of approximately 950,000 unstructured polyhedral cells each. A steady, incompressible, laminar flow model was used to simulate the inhalation

portion of a human breathing cycle. Volumetric flow rates were varied to represent the full range of human nasal breathing. Lagrangian particle tracking was performed for inertial fibrous and spherical particles. The simulation procedure and results of these numerical experiments are presented in the subsequent sections of this paper.

Simulation procedure

Geometry preparation

The nasal airway begins at the nostril and contains the vestibule, valve, and main airway regions. The main airway consists of the olfactory bulb and three sets of meatuses and turbinate's (superior, middle, and inferior). The airway terminates at the entrance to the nasopharynx where the two passages combine. Therefore, humans each have two typically asymmetric nasal airways separated by a thin piece of cartilage known as the septum. A labeled image of the left and right airways of the subject used in this study can be seen in Figure 1. The four sinus cavities, i.e., the ethnoid, frontal, maxillary, and sphenoid sinuses are not considered as part of the nasal airway and were ignored in this study. Further description of nasal anatomy can be found in Gray (1918).

For this study, two novel nasal airway models were constructed. MRI scans of a human volunteer's nose were taken at the Lovelace Respiratory Research Institute, Albuquerque, NM. The volunteer was an anonymous adult male of mass 120.2 kg and height 181.6 cm. The data was stored as point cloud definitions of 2D coronal cross sections taken every 3 mm. This is the same model that was used in the early work of Shanley et al. (2008) for spherical particle deposition, and is used here for analyzing the transport and deposition of ellipsoidal fibers.

A labor-intensive method similar to that of Subrumanian et al. (1998) and Zamankhan et al. (2006) was employed to generate two models. Model I represents the left nasal airway and Model II represents the right nasal airway. The coronal cross sections were loaded into the CAD package, Mechanical Desktop (Autodesk, Inc., San Rafael CA) and a second-order interpolation was used to produce splines between neighboring points in each coronal slice. Key perimeter coordinates were identified and used to create adjoining surfaces between the slices. The final definition was exported into STL format.

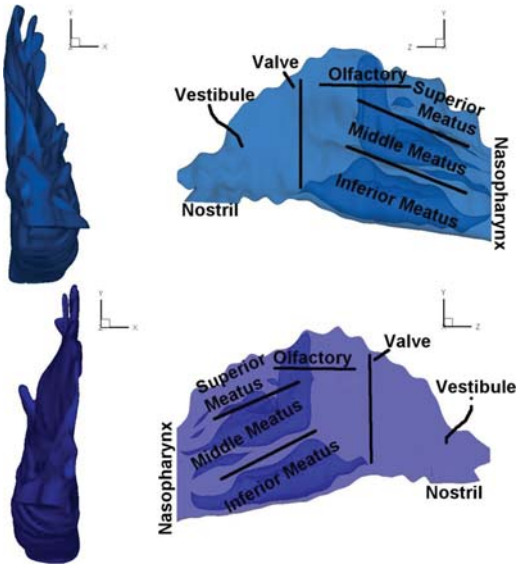

Figure 1. Labeled sagittal view of Model I (top) and Model II (bottom).

Grid preparation

Air travels through the nasal airway at velocities that are obviously incompressible, and the work of Liu et al. (2007) showed the flow field to be laminar. Here an unstructured mesh without near-wall prismatic layers was used. The mesh was largely comprised of tetrahedral elements with localized refinement and polyhedral elements used in areas of particular geometric complexity. Grid refinement was performed near the wall until the mesh independent solution was obtained. The resulting meshes totaled just less than one million cells for each model. An isometric view of a 3D volume mesh with 2D slice showing projected elements is presented in Figure 2. The following details the procedure for generating the mesh for CFD analysis.

The geometry resulting from the procedure described in section 2A consisted of a surface model with a minimal number of highly skewed triangle elements. While this representation may be highly desirable when building a rapid prototype model, smaller equilateral triangles are more conducive for preparing the geometry for CFD analysis. Therefore, the commercial software MagicsRP (Materialise Inc., Ann Arbor, MI) was used to retriangulate the surface. A split-based refinement was performed followed by a sharp edge smoothing. This procedure was an iterative process that terminated once improvement in mean triangle skewness could no longer be obtained.

A cluster of triangles were selected by hand to represent the inlet and exit of the domain (nostril and entrance to the nasopharynx, respectively). The selected triangles were extruded normal to their surface orientation and a planar cut was made. This step was performed to insure that there would be a smooth selectable surface for applying boundary conditions. The resulting model was exported in STL format.

The commercial software TGrid (ANSYS, Inc., Canonsburg, PA) was used to compute the mesh. A surface wrap procedure was performed to insure a water tight volume. Duplicate nodes were merged and unconnected nodes were deleted. The volume

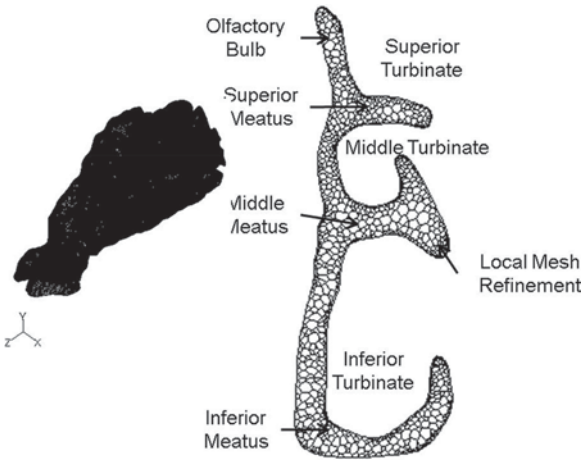

Figure 2. Isometric view of a volume mesh on Model I with 2D slice showing projected mesh elements in the main airway region of the nasal airway.

mesh was initialized to an unstructured tetrahedral mesh and a number of refinements and smoothing were performed to obtain a mesh that accurately represented the volume. The final mesh was imported into the ANSYS-FLUENT code.

Finally, tetrahedral cells were combined into polyhedral cells in areas of rapid geometric change. This was done to improve the overall quality of the mesh while maintaining the geometric integrity of the model. FLUENT (ANSYS, Inc., Canonsburg, PA) was used to complete this task. This task was rather straightforward and automated. FLUENT has an algorithm for performing this task without any additional input from the user once the option was selected. Once completed, the boundary conditions were applied and a FLUENT case file was written. The process for generating the computational mesh is shown schematically in Figure 3.

Figure 2 shows a volume mesh of Model I and a 2D slice with projected mesh elements. Close observation reveals localized refinement near the walls and in areas of high curvature. The studies of Vinchurkar and Longest (2008) and Dastan, Abouali, and Ahmadi (2014) suggest that use of hybrid mesh with near-wall prisms would improve the accuracy and reduce the overall number of needed grid.

Airflow simulations

The commercial software ANSYS-FLUENT (ANSYS, Inc., Canonsburg, PA) was used to perform CFD analysis. FLUENT employs the finite volume method to evaluate the partial differential equations governing fluid flow. The pressure-based solver was used with pressure–velocity coupling addressed by the semi-implicit method for pressure-linked equations (SIMPLE). Gradients were calculated via the Green–Gauss Node-Based Method, and the Second-Order Upwind differencing scheme was used.

A steady-state inhalation flow was assumed. Earlier, Shi, Kleinstreuer, and Zhang (2006) showed that the steady inhalation assumption leads to particle deposition results that are consistent with unsteady, periodic, breathing conditions. Boundary conditions were applied as a constant velocity with uniform profile (Keyhani, Scherer, and Mozell 1995) at the inlet surface and a constant static pressure on the exit surface (the so-called pressure outlet). The velocity at the inlet surface of each model was varied to achieve flow rates ranging from 2 L/min (sleeping) to 20 L/min (high exertion) in 2 L/min increments. The outlet pressure was set to sea-level static pressure (101.325 kPa) for each case.

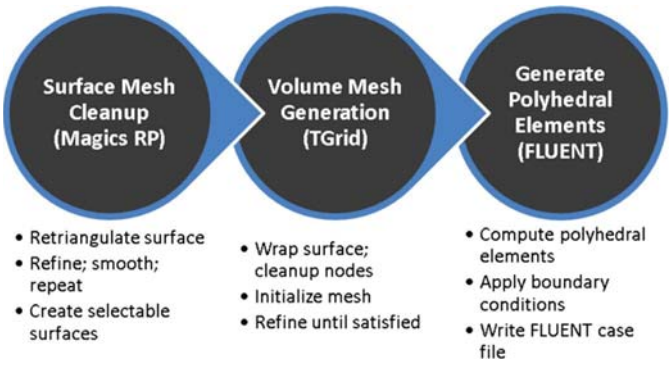

Figure 3. Process outline for generating computational mesh.

Lagrangian particle tracking

For the purposes of this study, fibers are assumed to be rigid ellipsoids, which is appropriate for materials such as asbestos and man made vitreous fibers (MMVF). To determine the behavior of fibers in the nasal airway the User Defined Function developed by Shanley and Ahmadi (2011) was used. This code provides a series of functions that augment the Discrete Phase Model (DPM) in ANSYS-FLUENT to include the dynamics of a rigid ellipsoid suspended in a fluid as described by Asgharian and Anjilvel (1995).

Figure 4 shows a flowchart of the steps taken to augment FLUENT Code for fiber transport and deposition analysis. Shanley and Ahmadi (2011) provided the details of the development, implementation, and validation of the User Defined Function (UDF). Therefore, there is no need to repeat those descriptions here. A synopsis of the mathematical expressions can be found in the appendix.

A one-way coupling assumption was made to simplify the particle tracking calculations. One-way coupling means that the fluid acts upon the particles to transport them, but the fluid is not disturbed by the presence of the particles and no particle is aware of the other particles. This assumption was reasonable given the dilute concentrations typically inhaled through the nose. Once the steady-state fluid solution was solved, the particle tracking was performed as a post-processing step.

For each airflow field obtained, a number of trials were run to vary particle parameters. The minor axis of the ellipsoid was varied from 1 to 10 μm, the density was varied from 1 to 3 g/cm^3, and the aspect ratio was varied from 5 to 15. In

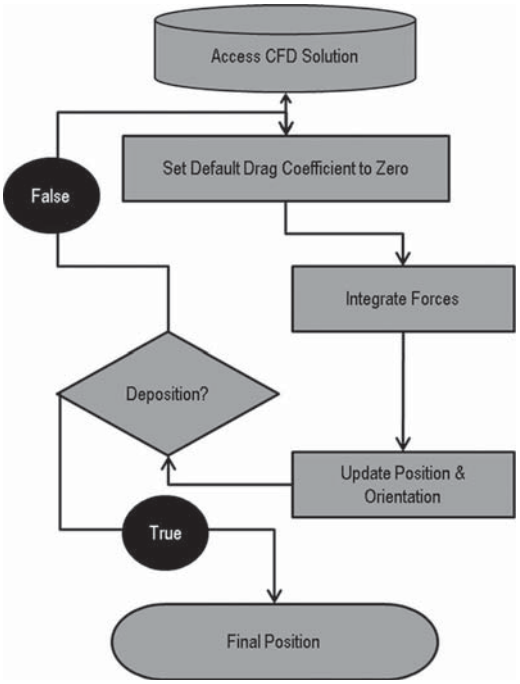

Figure 4. Flowchart illustrating the procedure for incorporating fiber tracking into the FLUENT DPM.

addition, separate simulations were conducted for spherical particles having an equivalent aerodynamic diameter corresponding to a fiber oriented with the long axis parallel to air flow as defined by Wang et al. (2008). That is,

$$d_{ae}^{f} = 3a^{f}\sqrt{\frac{\rho^{f}}{\rho^{\mathrm{H_2O}}}\left[Ln(2\beta) - 0.80685\right]}. \quad (1)$$

In Equation (1), a^f is the semi-minor axis of the ellipsoid, ρ^f is the density of the fiber, ρ^{H2O} is the density of water, and β is the aspect ratio of the fiber.

The FLUENT DPM was used to track these particles with the Stokes drag law and a Cunningham slip correction factor as computed as

$$C_c = 1 + \frac{2\lambda}{d}\left[1.257 + 0.4e^{-1.1d/\lambda}\right]. \quad (2)$$

In Equation (2), d is the equivalent physical diameter and λ is the mean free path of the gas, in this case air. For each particle trial, a single particle was released from the center of each cell face on the nostril surface. This resulted in a total of 1257 particles released in each trial.

Results and discussion

Airflow analysis

A series of CFD analyses were performed to help describe the airflow inside the two nasal airway models representing the left and right passages of a single subject. Steady-state, laminar, incompressible flow was assumed and only inhalation was addressed. The results of the simulations are presented in this section along with an empirical expression to describe the pressure drop in the human nasal airway in terms of Rohrer's equation.

Figure 5 shows the velocity magnitude on the primary vertical axis as a function of axial distance from the tip of the nose normalized by the length of the airway for Model I at a flow rate of 10 L/min. Here, the axial distance and length are taken parallel to the z-axis or straight down as the subject lies flat on his back. The velocity magnitude quantities are area weighted averages on coronal planes. Also shown on a secondary vertical axis in Figure 5 is the area of the coronal planes on which the velocity magnitude was computed. The peak in velocity was observed to be in the vestibule where the flow is accelerating due to turning. Throughout the rest of the airway, the velocity increased where the area shrunk and decreased where the area expanded. A secondary peak was observed in the valve at the point of minimum area. Here the air has completed its turn and the velocity was largely composed of its axial component.

Figure 6 shows contour plots of the axial velocity in the coronal sections analyzed for Figure 5. Careful investigation revealed the peak occurred at the valve with slightly lower axial velocity in the localized area in the coronal section immediately posterior to the valve. Qualitatively, these results were physically realistic and showed good agreement with previously published data (e.g., Swift and Proctor 1977; Kelly et al. 2004a, 2004b; Zamankhan et al. 2006; Shanley et al. 2008). Swift and Proctor (1977) reported observing recirculation immediately posterior to the nasal valve. This observation was not observed in the present study.

Figure 7 shows streamlines injected from the nostril surface and traced through the volume for both models at a moderate flow rate of 12 L/min No recirculation was observed for any streamline immediately posterior to the valve. However, a small recirculation was observed in the far posterior of the olfactory bulb in Model I. This recirculation was not present for very low or very high flow rates. Both models showed a recirculation in the vestibule under all flow rates. Recirculation is likely very sensitive to anatomy where small variations may generate, eliminate, or shift the presence of recirculation.

Figure 8 shows the pressure drop as a function of flow rate for both models. While both models showed very similar pressure loss characteristics, Model II showed consistently higher loss across the range of flow rates investigated. Also shown in Figure 8 is an empirical model taking the form of Rohrer's equation given by

$$\Delta p = k_1 Q^2 + k_2 Q. \quad (3)$$

In Equation (3), Q is the volumetric flow rate in L/min, $k_1 = 0.0859$ Pa/(L/min)^2, and $k_2 = 1.2906$ Pa/(L/min).

Figure 8 is consistent with k_2 being two orders of magnitude larger than k_1. The model given by (3) fits the simulation results for pressure drop–flow rate correlation for nasal Models I and II with an $R^2 = 0.9978$, which corresponds to a

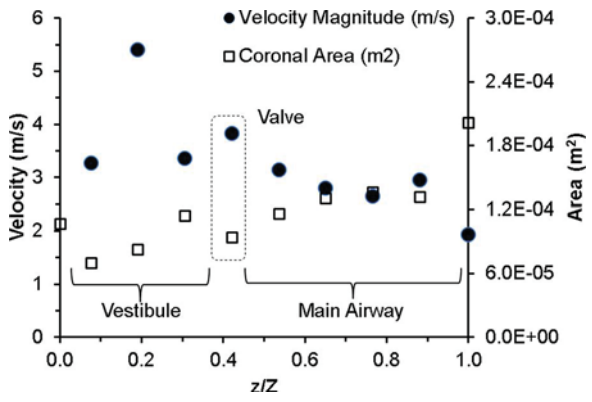

Figure 5. Velocity magnitude (primary vertical axis) and coronal area (secondary vertical axis) as a function of normalized axial distance through the airway.

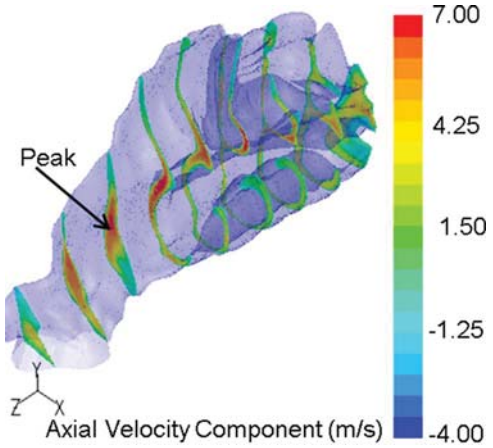

Figure 6. Axial velocity contours on coronal planes throughout the airway of Model I for a volumetric flow rate of 20 L/min.

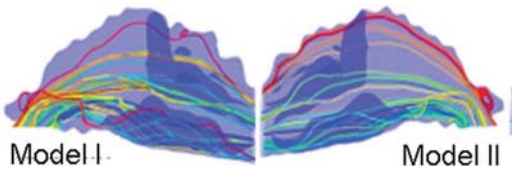

Figure 7. Streamlines injected from the nostril surface colored by path ID for Models I and II under a mass flow rate of 12 L/min.

very good agreement. While Equation (3) with the estimated coefficients seems to well describe the pressure–flow rate variations for Models 1 and II, exploring its application to other nasal passages need to be further explored. Such a study, however, is left for a future work.

Lagrangian particle tracking

Lagrangian particle tracking was performed to predict particle deposition efficiency in the nasal passages given the airflow fields described earlier. A uniform concentration of particles was introduced at the nostril surface for diameters ranging from 1 to 10 μm and densities from 1 to 3 g/cm^3. The aspect ratio was varied from 1 (spheres) to 15, and all fibers were aligned with the flow upon entry into the airway. For the dilute concentrations studied, a one-way coupling assumption was made. Deposition was assumed to occur upon contact with a wall boundary. The deposition efficiency was defined as the number of particles deposited on walls divided by the number of particles introduced at the nostril (inlet).

Figure 9 shows fiber deposition efficiency as a function of aspect ratio. The plot includes data from both models with a moderate and large minor axis (i.e., 4 and 10 μm).

Figure 9a shows data from a relatively low breathing rate of 4 L/min and Figure 9b shows data from a relatively high flow rate of 16 L/min. In order to highlight the effect of aspect ratio on the deposition efficiency, the results for particles with a density of 1 g/cm^3 are only shown in Figure 9. A nearly linear relationship was observed between deposition efficiency and aspect ratio except for the case with flow rate of 16 L/min and minor axis length of 10 μm where all of these fibers were deposited. Fibers having minor axis length of 10 μm deposited more frequently than those with minor axis length of 4 μm. The difference was less pronounced for a flow rate of 16 L/min because the momentum provided by the flow was the dominant deposition mechanism. For lower flow rates and lower minor axis lengths (i.e., 4 L/min and 4 μm), the deposition efficiency between the two models was nearly indistinguishable. However, Model I showed consistently higher deposition efficiency for both 4 L/min flow rate and 4 μm minor axis length, and 16 L/min flow rate and 4 μm minor axis length.

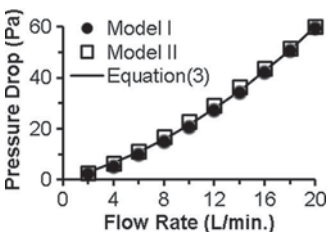

Figure 8. Pressure drop as a function of flow rate for Models I and II including fitted empirical model.

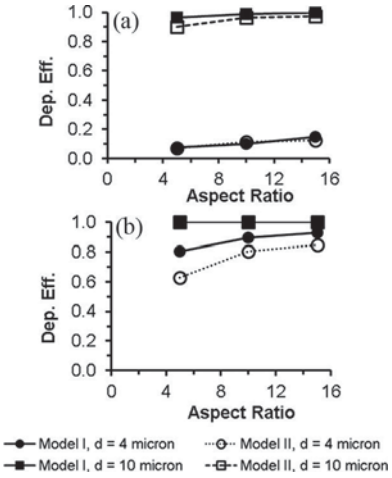

Figure 9. Particle deposition efficiency as a function of aspect ratio for (a) 4 L/min and (b) 16 L/min flow rates.

Figure 9 shows that deposition efficiency depends on aspect ratio, minor axis length, breathing rate, and the nasal anatomy. The aerodynamic diameter as defined in Equation (1) was used to collapse aspect ratio, minor axis length, and particle density into a single composite variable.

Figure 10 shows the deposition efficiency plotted as a function of the aerodynamic diameter for Model I. Also shown in Figure 10 is the deposition efficiency for spheres with equivalent aerodynamic diameters. Figure 10a shows the results for a flow rate of 4 L/min and Figure 10b shows results

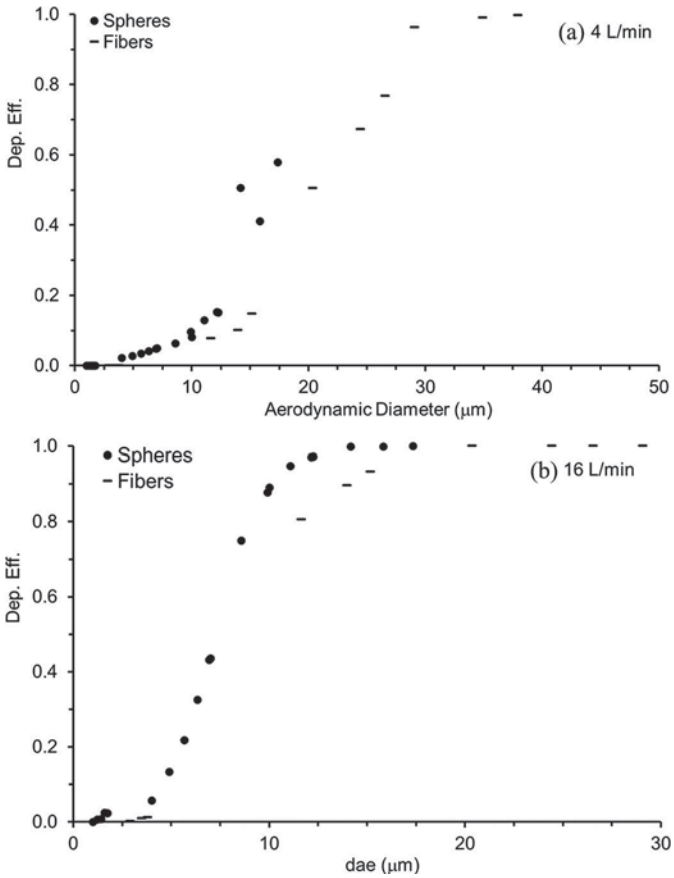

Figure 10. Particle deposition efficiency as a function of aerodynamic diameter for (a) 4 L/min and (b) 16 L/min flow rates.

for a flow rate of 16 L/min. At the lower flow rate, the fibers showed slightly higher deposition efficiency while at the higher flow rate fibers showed significantly lower deposition efficiency. As explained in Shanley and Ahmadi (2011), fibers are more stable under higher flow rates. Therefore, they do not rotate as frequently and remain aligned with the direction of the bulk flow. This behavior allows them to pass closer to the walls without depositing, than spheres with an equivalent aerodynamic diameter. Conversely, at lower flow rates, fibers are less stable and more likely to rotate that causes them to contact the wall more frequently than spheres with an equivalent aerodynamic diameter. Reviewing Figures 9 and 10 revealed that flow rate was a critical deposition parameter. The impaction parameter (IP $= d_{ae}^2 Q$) was used to incorporate the effects of flow rate on deposition efficiency.

Figure 11 shows the deposition efficiency plotted as a function of IP for both fibers and equivalent diameter spheres in both models. The entire data set is plotted in Figure 11 along with some previously published experimental and numerical studies (i.e., Kelly et al., 2004a; Su and Cheng 2005; Shanley et al. 2008). The general trend of the data agreed quite well with these other studies that included spheres (Kelly et al. 2004a; Shanley et al. 2008) and fibers (Su and Cheng 2005). (Note that the results of Shanely et al. (2008) were re-evaluated by a newer version of Ansys-fluent code and are slightly different from the original data.) In the steep part of the curve, each model falls into its own curve. The data from Shanley et al. (2008) had the highest deposition efficiency while the data from Model II of this study with fibers had the lowest deposition efficiency. Consistently, fibers had lower deposition efficiency than equivalent diameter spheres for both models. The distinct offset between each model plotted on Figure 11 implies that anatomy is a key element of the overall deposition rate.

A dimensionless Stokes number (*Stk*) was proposed by Cheng (2003) as a composite variable to describe nasal deposition efficiency of spheres in various human nasal airways. That is,

$$Stk = \frac{\sqrt{\pi} S d^2 Q}{18 \nu A_C^{1.5}}. \tag{4}$$

In Equation (4), S is the ratio of particle density to gas density, d is the diameter of the sphere in m, Q is the volumetric flow rate of the gas in m^3/s, μ is the dynamic viscosity of the gas in $kg/(m \cdot s)$, ν is the air kinematic viscosity (m^2/s), and A_C is the critical dimension proposed to be the area of the valve in m^2. Shanley et al. (2008) proposed an empirical expression to describe the deposition efficiency of spheres in nasal airways that vary with the inverse exponential square of *Stk*. That is,

$$E_d = 1 - \exp\{-\alpha_1 Stk^2\}. \tag{5}$$

In Equation (5), E_d is the deposition efficiency and α_1 is an empirical constant with the value of 250. The definitions in Equations (4) and (5) proved to be inadequate for the fiber simulation data in this study. Therefore, a new set of definitions are proposed. First, leveraging the technique of Wang et al. (2008), the critical dimension was separated into two key parameters (i.e., the area of the nostril surface and the hydraulic diameter of the valve). Thus, the Stokes number can be written as

$$Stk = \frac{\rho^{H_2O} d_{ae}^2}{18 \mu d_{h,\text{valve}}} \frac{Q}{A_{\text{nostril}}} = \frac{\rho^p d^2}{18 \mu d_{h,\text{valve}}} \frac{Q}{A_{\text{nostril}}}. \tag{6}$$

In Equation (6), ρ^{H2O} is the density of water in kg/m^3, ρ^p is the density of particle, d_{ae} is the aerodynamic diameter of the particle in m (fiber or sphere), Q is the volumetric flow rate of the gas in m^3/s, A_{nostril} is the cross-sectional area of the nostril surface in m^2, $d_{h,\text{valve}}$ is the hydraulic diameter of the nasal valve in m, which is the minimum cross-sectional area, and μ is the dynamic viscosity of the gas in kg/(m s).

To achieve a more robust empirical expression for particulate deposition in the human nasal airway, Equation (5) is recast into the following form:

$$E_d = 1 - \exp\{-\alpha_1 Stk^{\alpha_2}\}. \tag{7}$$

In Equation (7), the empirical constants are evaluated as $\alpha_1 = 8.88$ and $\alpha_2 = 1.61$, as determined by the data collected in this study. Treating the exponent as an empirical constant provided the model with an added level of flexibility to more accurately capture the shape of the data, which was not possible by the other proposed models. Furthermore, splitting the critical dimension into the nostril surface area and the valve hydraulic diameter imparts greater geometric detail into the Stokes number.

Figure 12 shows the deposition efficiency plotted as a function of the dimensionless Stokes number as defined by Equation (6) for both models and the data of Shanley et al. (2008) for spherical particles. Incorporating an anatomical feature through the *Stk* parameter helps to reduce the differences for individual nasal passages observed on Figure 11. Equation (7) is also plotted in Figure 12 for comparison. While there is some scatter in the data, the general agreement with the proposed empirical equations is reasonably good with a mean square error of 7.47×10^{-3}.

Recently Dastan, Abouali, and Ahmadi (2014) use several Stokes numbers based on the suggestions of Wang et al. (2008) and the earlier recommendation of Fan and Ahmadi (1995). They concluded that the Stokes number-based equivalent sphere diameter obtained from the translation dyadic averaged of Fan and Ahmadi (1995) is most promising for bringing the data for elongated fibers and spheres. Here we used only the

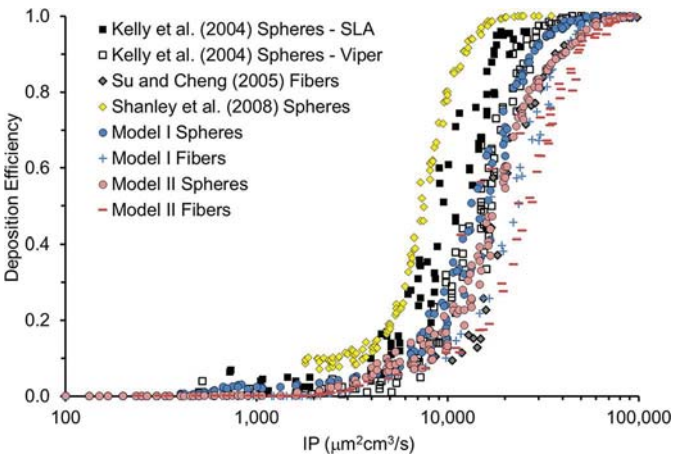

Figure 11. Deposition efficiency as a function of impaction parameter for spheres and fibers in both models along with previously published data.

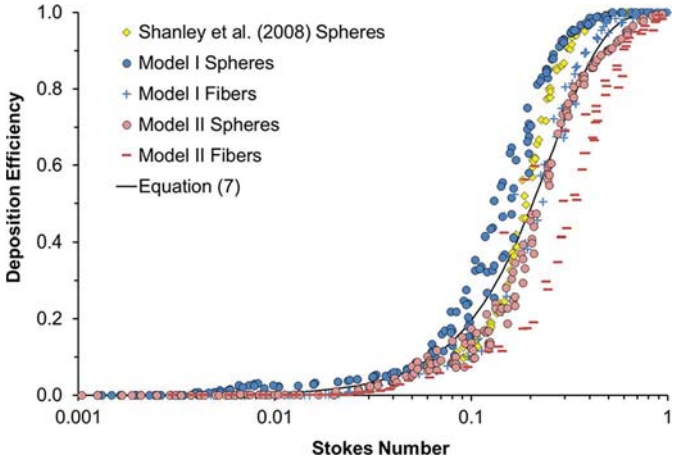

Figure 12. Deposition efficiency as a function of Stokes number for spheres and fibers in both models.

Stokes number based on the first suggestion of Wang et al. (2008) since the elongated fibers do stay parallel to the wall in most of their flight. Performing additional studies for finding a universal Stokes number that collapses the deposition data for elongated fibers and spherical particles to a single curve are left for a future study.

Summary and conclusions

The commercial CFD solver FLUENT-ANSYS was used to simulate the airflow and particle transport inside a human nasal airway model. Laminar, incompressible, and steady inhalation flow was assumed. Direct Lagrangian particle tracking was performed. The FLUENT DPM with a Stokes drag law was used to track spheres. A series of UDFs developed by Shanley and Ahmadi (2011) coupled with the FLUENT DPM was used to track coupled translational and rotation motions of fibers of different sizes and aspect ratio.

Simulation results show that the airflow velocity values showed a peak in the vestibule where it was undergoing substantial turning, and the axial component reached a peak in the nasal valve where the coronal area reaches a minimum. Streamlines were smoothly varying with the only significant recirculation occurring in the vestibule of each nasal model. Particle deposition was shown to depend on particle size and shape, flow rate, and anatomy. In general, fibers deposited with less frequency than equivalent diameter spheres because fibers remain aligned with the direction of the bulk flow (Shanley and Ahmadi 2011).

Two new empirical models pressure drop and particle and fiber deposition were developed and discussed. Equation (3) was proposed for the pressure loss through the nasal airway as a function of volumetric airflow rate. Pressure loss is a key parameter for understanding airflow in nasal airways. It is important to calculate this quantity without having to perform an invasive procedure. Equation (7) was proposed as an empirical model to predict the deposition efficiency of both fibers and spheres breathed through the nose. This model coupled with localized concentration data provides decision-makers with critical information to protect the safety of workers and residents. It does require information specific to the individual, but both the nostril surface area and valve hydraulic diameter may be obtained in a noninvasive way via imaging technology.

Acknowledgments

The authors are grateful for the support provided by Dr. Marcus Braun (ANSYS, Inc.) with development of the UDFs used here for tracking fibers.

Disclaimer

This work has not been subjected to either Agencies' required peer or policy review and therefore does not necessarily reflect the views of the agencies and no official endorsement shall be inferred.

Funding

The authors would like to gratefully acknowledge the financial support of the National Institute for Occupational Safety and Health (NIOSH) through Grant R01 OH003900.

ORCID

Philip K. Hopke http://orcid.org/0000-0003-2367-9661

References

Abouali, O., E. Erfan Keshavarzian, P. Farhadi Ghalati, A. Faramarzi, G. Ahmadi, and M. Hadi Bagheri. 2012. Micro and nanoparticle deposition in human nasal passage pre and post virtual maxillary sinus endoscopic surgery. *Respiratory Physiology & Neurobiology* 181:335–45. doi:10.1016/j.resp.2012.03.002.

Asgharian, B., and S. Anjilvel. 1995. The effects of fiber inertia on its orientation in a shear flow with application to lung dosimetry. *Aerosol Science and Technology* 23:282–90. doi:10.1080/02786829508965313.

Cheng, Y. S. 2003. Aerosol deposition in the extrathoracic region. *Aerosol Science and Technology* 37:659–71. doi:10.1080/02786820300906.

Cheng, Y. S., C. Fu, D. Yazzie, and Y. Zhou. 2001a. Respiratory deposition patterns of salbutamol pMDI with CFC and HFA-134a formulations in a human airway replica. *Journal of Aerosol Medicine* 14:255–66. doi:10.1089/08942680152484180

Cheng, Y. S., T. D. Holmes, J. Gao, R. A. Guilmette, S. Li, Y. Surakitbanharn, and C. Rowlings. 2001b. Characterization of nasal spray pumps and deposition pattern in a replica of the human nasal airway. *Journal of Aerosol Medicine* 14:267–80. doi:10.1089/08942680152484199.

Dai, Y. T., Y.-J. Juang, Y. Wu, P. N. Breysse, and D.-J. Hsu. 2006. In vivo measurements of inhalability of ultralarge aerosol particles in calm air by humans. *Journal of Aerosol Science* 37:967–73. doi:10.1016/j.jaerosci.2005.10.002.

Dastan, A., O. Abouali, and G. Ahmadi. 2014. CFD simulation of total and regional fiber deposition in human nasal cavities. *Journal of Aerosol Science* 69:132–49. doi:10.1016/j.jaerosci.2013.12.008.

Fan, F. G., and G. Ahmadi. 1995. A sublayer model for wall deposition of ellipsoidal particles in turbulent streams. *Journal of Aerosol Science* 26(5): 813–41. doi:10.1016/0021-8502(95)00021-4.

Ghahramani, E., O. Abouali, H. Emdad, and G. Ahmadi. 2014. Numerical analysis of stochastic dispersion of micro-particles in turbulent flows in a realistic model of human nasal/upper airway. *Journal of Aerosol Science* 67:188–206. doi:10.1016/j.jaerosci.2013.09.004.

Gray, H. 1918. *Anatomy of the human body*. Philadelphia, PA: Lea & Febiger.

Guilmette, R. A., Y. S. Cheng, H. C. Yeh, and D. L. Swift. 1994. Deposition of 0.005–12 μm monodisperse particles in a computer-milled, MRI-based nasal airway replica. *Inhaled Toxicology* 6(Suppl. 1): 395–99.

Guilmette, R. A., J. D. Wicks, and R. K. Wolff. 1989. Morphometry of human nasal airways in vivo using magnetic resonance imaging. *Journal of Aerosol Medicine* 2 (4):365–77. doi:10.1089/jam.1989.2.365.

Harper, E. Y., and Chang, Y. D. 1968. Maximum dissipation resulting from lift in a viscous shear flow. *Journal of Fluid Mechanics* 33 (2):209–25. doi:10.1017/s0022112068001254.

Inthavong, K., J. Wen, Z. Tian, and J. Tu. 2008. Numerical study of fibre deposition in a human nasal cavity. *Journal of Aerosol Science* 39:253–65. doi:10.1016/j.jaerosci.2007.11.007.

Kelly, J. T., B. Asgharian, J. S. Kimbel, and B. A. Wong. 2004a. Particle deposition in human nasal airway replicas manufactured by different methods. Part I: Inertial regime. *Aerosol Science and Technology* 38:1063–71. doi:10.1080/027868290883360.

Kelly, J. T., B. A. Asgharian, J. S. Kimbell, and B. A. Wong. 2004b. Particle deposition in human nasal airway replicas manufactured by different methods. Part II: Ultrafine particles. *Aerosol Science and Technology* 38:1072–79. doi:10.1080/027868290883432.

Kelly, J. T., A. K. Prasad, and A. S. Wexler. 2000. Detailed flow patterns in the nasal cavity. *Journal of Applied Physiology* 89:323–37.

Keyhani, K., P. W. Scherer, and M. M. Mozell. 1995. Numerical simulation of airflow in the human nasal cavity. *Journal of Biomechanical Engineering* 117:429–41. doi:10.1115/1.2794204.

Liu, Y., E. A. Matida, J. Gu, and M. R. Johnson. 2007. Numerical simulation of aerosol deposition in a 3-D human nasal cavity using RANS, RANS/EIM, and LES. *Journal of Aerosol Science* 38:683–700. doi:10.1016/j.jaerosci.2007.05.003.

Moghadas, H., O. Abouali, A. Faramarzi, and G. Ahmadi. 2011. Numerical investigation of septal deviation effect on deposition of nano/microparticles in human nasal passage. *Respiratory Physiology and Neurobiology* 177:9–18. doi:10.1016/j.resp.2011.02.011.

Pope III, C. A. 2000. Review: Epidemiological basis for particulate air pollution health standards. *Aerosol Science and Technology* 32:4–14. doi:10.1080/027868200303885.

Saffman, P. G. 1965. The lift on a small sphere in a slow shear flow. *Journal of Fluid Mechanics* 22 (2):385–400. doi:10.1017/s0022112065000824.

Shanley, K. T., and G. Ahmadi. 2011. A numerical model for simulating the motions of ellipsoidal fibers in low Reynolds number shear flows. *Aerosol Science and Technology* 45 (7):838–48. doi:10.1080/02786826.2011.566293.

Shanley, K. T., P. Zamankhan, G. Ahmadi, P. K. Hopke, and Y. S. Chang. 2008. Numerical simulations investigating the regional and overall deposition efficiency of the human nasal cavity. *Inhalation Toxicology* 20 (12):1093–100. doi:10.1080/08958370802130379.

Shi, H., C. Kleinstreuer, and Z. Zhang. 2006. Laminar airflow and nanoparticle or vapor deposition in a human nasal cavity model. *Journal of Biomechanical Engineering* 128:697–706. doi:10.1115/1.2244574.

Shi, H., C. Kleinstreuer, and Z. Zhang. 2007. Modeling of inertial particle transport and deposition in human nasal cavities with wall roughness. *Journal of Aerosol Science* 38:398–419. doi:10.1016/j.jaerosci.2007.02.002.

Shi, H., C. Kleinstreuer, and Z. Zhang. 2008. Dilute suspension flow with nanoparticle deposition in a representative nasal airway model. *Physics of Fluids* 21:197–208.

Su, W. C., and Y. S. Cheng. 2005. Deposition of fiber in the human nasal airway. *Aerosol Science and Technology* 39:888–901. doi:10.1080/02786820500295685.

Su, W. C., J. Wu, J. C. M. Marijmissen, and Y. S. Cheng. 2008. Deposition of man-made fibers in a human nasal airway. *Aerosol Science and Technology* 42:173–81. doi:10.1080/02786820801922938.

Subramanian, R. P., R. B. Richardson, K. T. Morgan, J. S. Kimbell, and R. A. Guilmette. 1998. Computational fluid dynamics simulations of inspiratory airflow in the human nose and nasopharynx. *Inhalation Toxicology* 10:91–120. doi:10.1080/089583798197772.

Swift, D. L. 1991. Inspiratory inertial deposition of aerosols in human nasal casts: Implications for the proposed NCRP lung model. *Radiation Protection Dosimetry* 38:29–34.

Swift, D. L., Montassier, N., Hopke, P. K., Karpen-Hayes, K., Cheng, Y. S., Su, Y. F., and Strong, J. C. 1992. Inspiratory deposition of ultrafine particles in human nasal replicate cast. *Journal of aerosol science* 23 (1):65–72.

Swift, D. L., and D. F. Proctor. 1977. Access of air to the respiratory tract. In *Respiratory defense mechanisms: Part I*, ed. J. D. Brian D. F. Proctor and L. M. Reid 63–93. New York, NY: Dekker.

Tu, J. Y., K. Inthavong, and G. Ahmadi. 2013. *Fluid particle dynamics of the human respiratory system – A computational approach*. New York, NY: Springer.

U.S. Environmental Protection Agency [USEPA]. 1996. *Air quality criteria for particulate matter*. Washington, DC: U.S. Environmental Protection Agency.

Vinchurkar, S., and P. W. Longest. 2008. Evaluation of hexahedral, prismatic and hybrid mesh styles for simulating respiratory aerosol dynamics. *Computer and Fluids* 37:317–31. doi:10.1016/j.compfluid.2007.05.001.

Wang, Z., P. K. Hopke, G. Ahmadi, Y.-S. Cheng, and P. A. Baron. 2008. Fibrous particle deposition in human nasal passage: The influence of particle length, flow rate, and geometry of nasal airway. *Journal of Aerosol Science* 39:1040–54. doi:10.1016/j.jaerosci.2008.07.008.

Zamankhan, P., G. Ahmadi, Z. Wang, P. K. Hopke, Y.-S. Cheng, W. C. Su, and D. Leonard. 2006. Airflow and deposition of nano-particles in a human nasal cavity. *Aerosol Science and Technology* 40:463–76. doi:10.1080/02786820600660903.

Appendix

A detailed description of the equations of motion and the implementation in ANSYS-FLUENT was presented by Shanley and Ahmadi (2011) and the theoretical background was reported by Asgharian and Anjilvel (1995). This appendix provides a brief summary for the governing equations. Additional details may be found in the references.

The equations of translational and rotational motions of rigid fibers are coupled, and are given as

$$m_p \frac{d\mathbf{v}}{dt} = \mathbf{F_D} + \mathbf{F}_L + (m_p - m)\mathbf{g}, \tag{A.1}$$

$$\frac{d}{dt}(\mathbf{I_M} \cdot \boldsymbol{\omega}) = \mathbf{T_h}. \tag{A.2}$$

Equation (A.1) describes the translational motion of the center of the mass of a fiber (rigid body). Here v is the particle velocity vector, t is the time, m_p is the fiber mass, and m is the mass of equivalent volume air (typically neglected). The forces on the right-hand side of (A.1) are hydrodynamic drag ($\mathbf{F_D}$), shear-induced lift ($\mathbf{F}_L$), and gravity including buoyancy. Equation (A.2) describes the rotational motion of the fiber (rigid body) generated by the hydrodynamic torque (T_h) exerted on the fiber. Here $\mathbf{I}_M$ is the mass moment of inertia tensor and ω is the angular velocity of the fiber.

The hydrodynamic drag acting on a fiber depends on the orientation of the fiber and airflow Reynolds number around the fiber. The mathematical expression for the hydrodynamic drag is given as

$$\mathbf{F_D} = \pi \mu d \mathbf{K} \cdot (\mathbf{u} - \mathbf{v}). \tag{A.3}$$

Here d is the cross-sectional diameter or minor axis of the fiber, $\mathbf{u}$ is the air flow velocity, μ is the fluid (air) dynamic viscosity, and $\mathbf{K}$ is the translational dyadic. Solving Equations (A.1) and (A.2), Asgharian and Anjilvel (1995) evaluated the expression for the angular acceleration for the fiber. The components of which are

$$\begin{aligned}\frac{d^2\varphi}{dt^2} = {} & \frac{2}{(\beta^2+1)\sin\theta}\frac{d\theta}{dt}\left[\frac{d\psi}{dt} - \beta^2\cos\theta\frac{d\varphi}{dt}\right] \\ & + \frac{\mu}{\rho d^2}\frac{20}{\beta(\gamma_0+\beta^2\alpha_0)}\cdot\left\{\left[(\zeta\cos\varphi - \eta\sin\varphi)\cot\theta + \xi - \frac{d\varphi}{dt}\right]\right. \\ & + \frac{\beta^2-1}{\beta^2+1}\left[\left(d_{xy}\cos\varphi + d_{xz}\sin\varphi\right)\cot\theta\right. \\ & \left.\left. - d_{yz}\cos 2\varphi + \frac{1}{2}\left(d_{yy} - d_{zz}\right)\sin 2\varphi\right]\right\},\end{aligned} \tag{A.4}$$

$$\frac{d^2\theta}{dt^2} = -\frac{2}{(\beta^2+1)}\frac{d\varphi}{dt}\left[\frac{d\psi}{dt}\sin\theta + \frac{1}{4}(\beta^2-3)\sin 2\theta\frac{d\varphi}{dt}\right] + \frac{\mu}{\rho d^2}\frac{20}{\beta(\gamma_0+\beta^2\alpha_0)}\cdot\left\{\left[\eta\cos\varphi+\zeta\sin\varphi-\frac{d\theta}{dt}\right] - \frac{\beta^2-1}{\beta^2+1}\left[(d_{yz}\cos\varphi - d_{xy}\sin\varphi)\cos 2\theta + \frac{1}{2}\sin 2\theta\,(d_{xx}+d_{yz}\sin 2\varphi - d_{yy}\sin^2\theta - d_{zz}\cos^2\theta)\right]\right\}, \quad (A.5)$$

$$\frac{d^2\psi}{dt^2} = \frac{\cot\theta}{(\beta^2+1)}\frac{d\theta}{dt}\left[\left(\cos\theta + \frac{(\beta^2+1)}{(\beta^2-1)}\right)\frac{d\varphi}{dt} - 2\frac{d\psi}{dt}\right] + \frac{\mu}{\rho d^2}\frac{20\cos\theta}{\beta(\gamma_0+\beta^2\alpha_0)}\cdot\left\{\left[(\zeta\cos\varphi-\eta\sin\varphi)\cot\theta + \xi - \frac{d\phi}{dt}\right] + \frac{\beta^2-1}{\beta^2+1}\left[(d_{xy}\cos\varphi + d_{xz}\sin\varphi)\cot\theta - d_{yz}\cos 2\varphi + \frac{1}{2}(d_{yy}-d_{zz})\sin 2\varphi\right]\right\} + \frac{\mu}{\rho d^2}\frac{20\cos\theta}{\beta\gamma_0}\left\{\left(\xi - \frac{d\varphi}{dt}\right)\cos\theta + (\zeta\sin\varphi - \eta\cos\varphi)\sin\theta - \frac{d\psi}{dt}\right\} \quad (A.6)$$

In Equations (A.3)–(A.5), φ, θ, and ψ are the Euler angles, ρ is the density of the ellipsoid, and β is the aspect ratio of the ellipsoid.

For an ellipsoid of revolution suspended in a simple shear flow, the shear-induced lift can be expressed as

$$\mathbf{F_L} = \frac{\pi^2\mu d^2}{4\sqrt{\nu}}\frac{\partial\mathbf{u}/\partial y}{|\partial\mathbf{u}/\partial y|^{\frac{1}{2}}}(\mathbf{K}\cdot\mathbf{L}\cdot\mathbf{K})\cdot(\mathbf{u}-\mathbf{v}). \quad (A.7)$$

In Equation (A.7), ν is the kinematic viscosity of the fluid, y is a spatial coordinate, and $\mathbf{L}$ is the lift coefficient matrix described by Harper and Chang (1968) as

$$\mathbf{L} = \begin{pmatrix} 0.0501 & 0.0329 & 0.0000 \\ 0.0182 & 0.0173 & 0.0000 \\ 0.0000 & 0.0000 & 0.0373 \end{pmatrix}. \quad (A.8)$$

Equations (A.7) and (A.8) are the generalized form of Saffman (1965) lift force. Also an ellipsoid was considered to be deposited when any point on the ellipsoid intersected with the wall surfaces.

Interlibrary Loans and Journal Article Requests

Notice Warning Concerning Copyright Restrictions:

The copyright law of the United States (Title 17, United States Code) governs the making of photocopies or other reproductions of copyrighted materials.

Under certain conditions specified in the law, libraries and archives are authorized to furnish a photocopy or other reproduction. One specified condition is that the photocopy or reproduction is not to be *"used for any purpose other than private study, scholarship, or research."* If a user makes a request for, or later uses, a photocopy or reproduction for purposes in excess of "fair use," that user may be liable for copyright infringement.

Upon receipt of this reproduction of the publication you have requested, you understand that the publication may be protected by copyright law. You also understand that you are expected to comply with copyright law and to limit your use to one for private study, scholarship, or research and not to systematically reproduce or in any way make available multiple copies of the publication.

The Stephen B. Thacker CDC Library reserves the right to refuse to accept a copying order if, in its judgment, fulfillment of the order would involve violation of copyright law.

Terms and Conditions for items sent by e-mail:

The contents of the attached document may be protected by copyright law. The CDC copyright policy outlines the responsibilities and guidance related to the reproduction of copyrighted materials at CDC. If the document is protected by copyright law, the following restrictions apply:

- You may print only one paper copy, from which you may not make further copies, except as maybe allowed by law.
- You may not make further electronic copies or convert the file into any other format.
- You may not cut and paste or otherwise alter the text.